Excitation of ultrasharp trapped-mode resonances in mirror-symmetric metamaterials

Shengyan Yang,[1] Zhe Liu,[1] Xiaoxiang Xia,[1] Yiwen E,[1] Chengchun Tang,[1] Yujin Wang,[1] Junjie Li,[1] Li Wang,[1] and Changzhi Gu[1,2,*]

[1]*Beijing National Laboratory for Condensed Matter Physics, Institute of Physics, Chinese Academy of Sciences, Beijing 100190, China*

[2]*Collaborative Innovation Center of Quantum Matter, Beijing, China*

(Received 9 September 2015; revised manuscript received 15 April 2016; published 6 June 2016)

We experimentally demonstrate a metamaterial structure composed of two mirror-symmetric joint split ring resonators (JSRRs) that support extremely sharp trapped-mode resonance with a large modulation depth in the terahertz region. Contrary to the regular mirror-arranged SRR arrays in which both the subradiant inductive-capacitive (*LC*) resonance and quadrupole-mode resonance can be excited, our designed structure features a metallic microstrip bridging the adjacent SRRs, which leads to the emergence of an otherwise inaccessible ultrahigh-quality-factor resonance. The ultrasharp resonance occurs near the Wood-Rayleigh anomaly frequency, and the underlying mechanism can be attributed to the strong coupling between the in-plane propagating collective lattice surface mode originating from the array periodicity and localized surface plasmon resonance in mirror-symmetric coupled JSRRs, which dramatically reduces radiative damping. The ultrasharp resonance shows great potential for multifunctional applications such as plasmonic switching, low-power nonlinear processing, and chemical and biological sensing.

DOI: 10.1103/PhysRevB.93.235407

I. INTRODUCTION

Metamaterials (MMs) are artificial electromagnetic materials consisting of periodically arranged subwavelength resonators, which exhibit unusual and exotic properties that give rise to new capabilities in manipulating electromagnetic waves in a desired manner. The unique properties of metamaterials arise mainly from the resonant nature of their unit cell configuration and arrangement. Achieving sharp resonances with a high-quality factor (Q factor) is of significant importance in realizing ultrasensitive sensors [1–6], high performance filters [7–9], laser spaser [10,11], and slow light devices [12–16]. These applications require photonic structures characterized by their ultrasharp spectral responses and miniaturized scale. For instance, ultrasensitive real time chemical and biomolecular sensing could be achieved only by high Q factor resonances with extremely narrow linewidths, and the resonance with a high modulation depth will enhance the sensitivity in sensing applications [1,17,18]. Therefore, numerous efforts have been made to obtain sharp resonances and further optimize the sharpness and modulation depth of the resonances. However, conventional planar metamaterials generally suffer from a low Q factor and compromise the efficiency of metamaterial devices due to radiation and Joule losses. Comparing the two avenues of loss, the radiation losses at terahertz frequencies are dominant, as the Joule losses are generally quite low in most metals due to the excellent conductivity in this frequency regime [19–21]. Hence, the key to achieving high Q factor resonances is to greatly minimize the radiation losses.

One of the most common approaches to reducing radiation losses and achieving a high Q factor is to utilize asymmetric coupling between two directly excited bright modes, which can drive the current to oscillate out of phase and thus reduce radiation losses. Based on this method, several schemes have been proposed to suppress the losses and improve the Q factor in planar metamaterials, such as asymmetric split ring resonators (ASRs) [9,22–26], concentric ring resonators with interdigitated fingers (ICRs) [27], and D-split resonators [28]. Another approach to obtaining high Q factor resonances is to excite the dark modes that cannot be excited by a particular polarization. For example, Al-Naib *et al.* [29] demonstrated that conductively coupled split ring resonators (SRRs) could support a high Q resonance upon excitation of the dark modes that cannot be directly excited in individual SRRs when the electric field is perpendicular to the gaps of the SRRs. In this configuration, the large Q factor resonance could not be excited with the electric field parallel to the gaps of the SRRs, due to ultrahigh radiation losses. In addition, sharp resonances with a high Q factor can also be obtained via different coupling schemes to form metamolecules that consist of a group of SRRs [21,30,31]. Each method has its own merits, but demonstrating sharp metamaterial resonances with an ultrahigh Q factor and a large modulation depth has proven to be highly challenging, thus severely hindering the further progress of metamaterials in practical applications.

In this paper, we present a scheme to excite ultrasharp trapped-mode resonances with a large modulation depth by utilizing mirror-symmetric joint split ring resonators (JSRRs) operating on a diffraction coupling mechanism. In this structure, we observe a nearly complete cancellation of the net dipole moment, accompanied by strong suppression of radiative losses and thus an extremely sharp resonance at a certain critical periodicity p that matches the Wood-Rayleigh anomaly frequency. Intriguingly, when the periodicity is further reduced, a new high-order diffraction mode resonance emerges. Tailoring the periodicity of mirror-symmetric JSRR structures allows for the excitation of multiple sharp resonances with an adjustable Q factor for various applications. Moreover, we also demonstrate that the sharp trapped-mode resonance can be modulated by manipulating the gap position of each SRR. It is worth stressing that the design principle is essentially distinct from the asymmetric coupling between two

*Corresponding author: czgu@iphy.ac.cn

dark modes for achieving high Q resonance in Ref. [29]. The coupling mechanism we propose here provides an alternative path to excite extremely narrow plasmonic resonances with a large modulation depth across the entire electromagnetic spectrum, which holds promise for applications in the field of photonic devices.

II. STRUCTURAL DESIGN

In the conception of metamaterials, SRRs have arguably become fundamental building blocks, and various configurations have been proposed to manipulate the electromagnetic responses. In the present work, four SRR derivative samples were designed and fabricated. Figure 1(a) is a schematic of the conventional mirrored SRR (sample MM1) supercell, which consists of four completely identical SRRs that are mirror-arranged along the x and y axes. For sample MM2, shown in Fig. 1(b), we intentionally introduce metallic microstrip bridges to join the adjacent SRRs to form a mirror-symmetric JSRR unit cell. For sample MM3/MM4 supercells, shown in Figs. 1(c) and 1(d), the capacitive split gaps in the MM2 SRRs are displaced outboard/inboard by 10.5 μm from the central axes of each SRR, respectively. The planar metallic SRRs have the same dimension, with a side length of $l = 28\,\mu$m, a width of $w = 2\,\mu$m, a gap of $g = 3\,\mu$m, and supercell lattice constants of $p = p_x = p_y = 120\ \mu$m. In the JSRRs, the metallic microstrip bridge has a length of $2h = 32\,\mu$m, where h is the distance from the edge of each SRR to the y axis of the unit cell. The patterns were fabricated by high-resolution electron-beam lithography, followed by thermal evaporation of 200 nm gold and subsequently a lift-off procedure on a high-resistivity 1-mm-thick silicon substrate ($n = 3.45$). The fabricated metamaterial samples are characterized by terahertz time domain spectroscopy (THz-TDS) [32].

Numerical simulations are performed by the commercial simulation software FDTD Solutions based on the finite difference time-domain algorithm. The simulation domain includes one unit cell of the MMs with periodic boundary conditions in both the x and y directions. The simulation volume is discretized by grid meshes, and the mesh size is set down to 200 nm to ensure the accuracy of the calculated results. Perfectly matched layer boundary condition is used along the propagation of the electromagnetic waves (z axis). Plane waves are launched to the unit cell along the $+z$ direction with the x-polarization (parallel to the gap of SRR), and the absolute amplitude transmittance was obtained behind the unit cell. The surface current and electric field distributions are detected within the two-dimensional (2D) field profile monitors. In the simulations, the permittivity of gold was described by the Drude model, $\varepsilon(\omega) = 1 - \omega_p^2/(\omega^2 + i\gamma\omega)$, where ω_p is the plasma frequency and γ is the damping rate. For gold, the characteristic frequencies are taken as $\omega_p/2\pi = 2181$ THz and $\gamma/2\pi = 6.5$ THz [33,34]. The relative electrical permittivity of the silicon substrate is taken to be 11.9. The results are also reproduced by using another commercially available full-wave simulation tool, CST Microwave Studio, based on the finite integration method.

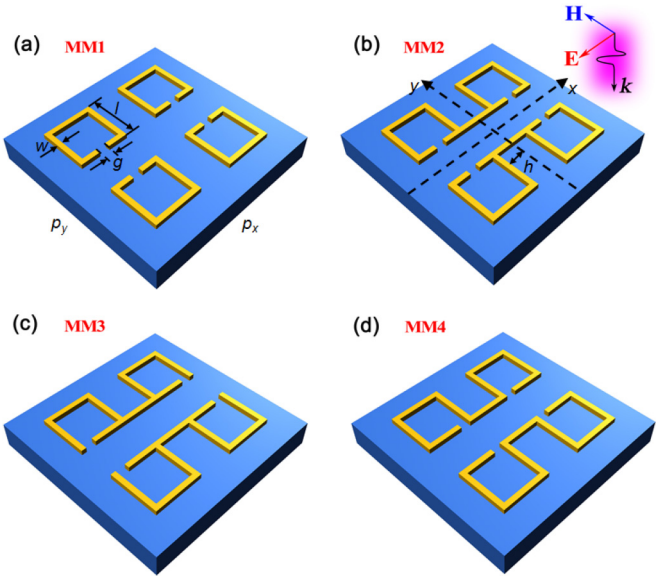

FIG. 1. Structural schematic of the proposed resonant structures with detailed geometric dimensions. (a) Sample MM1, (b) sample MM2, (c) sample MM3, and (d) sample MM4 supercells.

III. EXPERIMENTAL AND SIMULATED RESULTS

Figures 2(a)–2(d) show the scanning electron micrograph images of samples MM1, MM2, MM3, and MM4, while the corresponding measured and simulated transmission spectra for those samples are shown in Figs. 2(e)–2(h) and Figs. 2(i)–2(l), respectively. The polarization of the incident light is parallel to the gaps of the SRRs, as shown in the inset. Reasonable agreement is achieved between the simulations and the measurements, as all the resonant modes are reproduced in the measured curves with almost the same frequencies. The discrepancy in the sharpness of the resonances between the theory and the experiments can be attributed to the limited resolution of the measurements. In the case of MM1, we observe that the mirrored SRRs allow the formation of a subradiant LC resonance at 0.56 THz with antiphase currents in the vertically neighboring SRRs [31]. The Q factor, which is defined as the ratio of the central frequency to the full width at half maximum (FWHM) bandwidth of a resonance, is 18 for the subradiant LC resonance. It should be noted that the value is higher than that of the traditional nonmirror arranged SRRs [6,31]. At the same time, the quadrupole-mode resonance at 1.62 THz with a Q factor of 4 is also excited.

When the adjacent SRRs are joined by metallic microstrip bridges horizontally (MM2), as shown in Fig. 2(b), we observe an ultrasharp trapped-mode resonance that appears at $f_2 = 0.71$ THz in the simulated transmission spectrum, with a bandwidth of 11.8 GHz and a Q factor of 60, which is more than one order of magnitude higher than that of traditional dipole resonance [11,20]. Moreover, the resonance modulation depth $[1-T(f)]$ of the trapped-mode resonance f_2 reaches 57% [see Fig. 2(j)]. Obviously, this MM structure, combined with a high Q factor and large modulation depth, offers an effective way for ultrasensitive sensing and ultranarrow band filtering. Meanwhile, a broad resonant featured mode at $f_1 = 0.34$ THz is excited, which has a Q factor of 4, indicating a huge radiation loss. Additionally, the resonance frequency of the

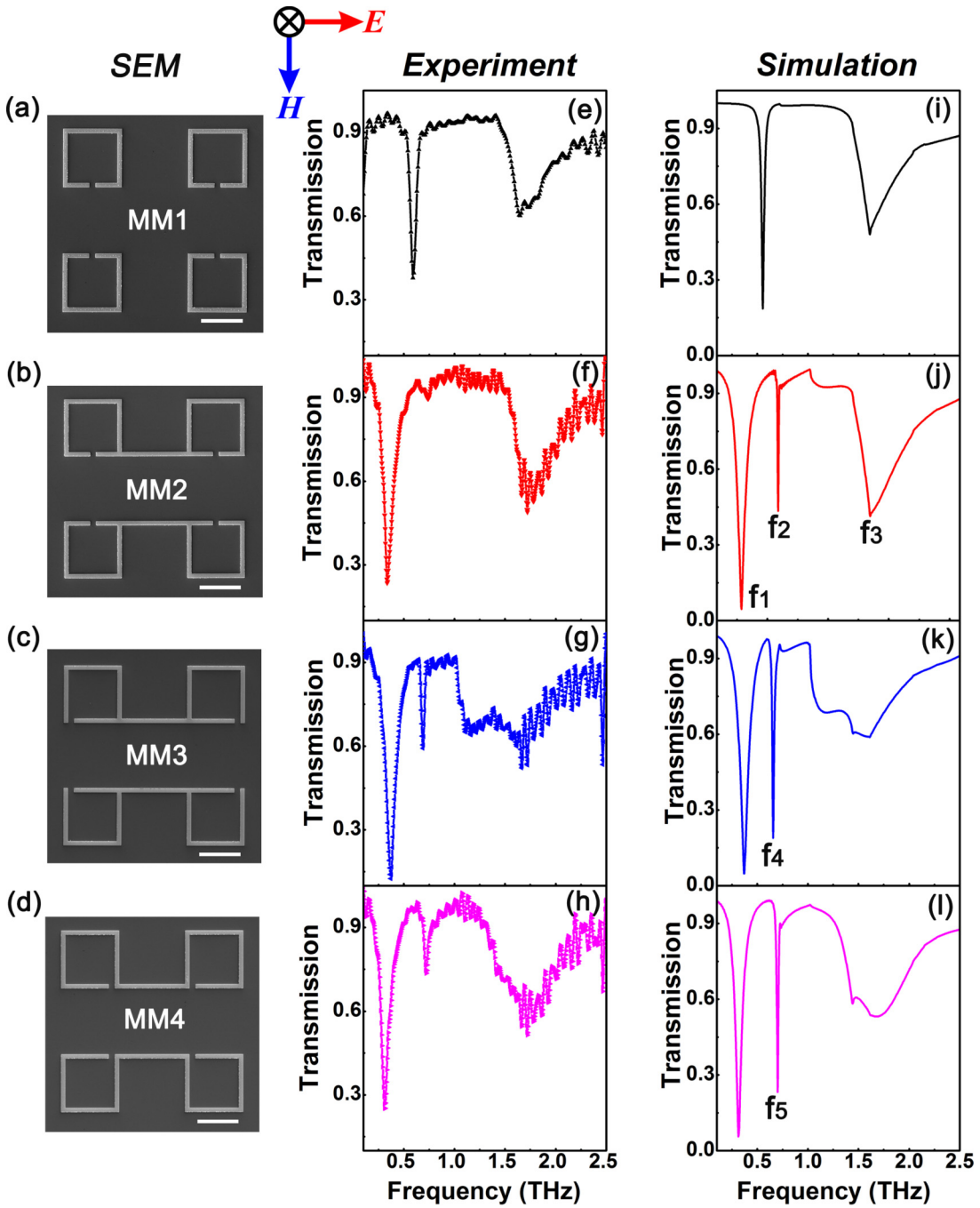

FIG. 2. Scanning electron microscopy (SEM) images of samples (a) MM1, (b) MM2, (c) MM3, and (d) MM4 are shown in the left column. The scale bar is 20 μm. The measured and simulated amplitude transmission spectra of the corresponding structures are shown in the middle and right columns, respectively. Insets depict the incident electric (E) and magnetic (H) field orientations.

quadrupole mode remains unchanged ($f_3 = 1.62$ THz). As for sample MM3, the sharp trapped-mode resonance becomes more prominent in Fig. 2(k) and shows a redshift to 0.65 THz. The resonance modulation depth for the resonance reaches up to 81%, while the Q factor decreases to 24. In contrast, for sample MM4, the sharp trapped-mode resonance appears at 0.7 THz in Fig. 2(l). The modulation depth for the resonance reaches 77%, and the Q factor decreases to 35. Conversely, for all the mirror-symmetric JSRR samples MM2–MM4, the measured Q factors of the trapped-mode resonances have much smaller values, around 20, due to the limited frequency resolution of the employed THz-TDS systems. From the theoretical results, the FWHM of the trapped-mode resonance f_2 is just 11.8 GHz. To achieve a frequency resolution of 11.8 GHz, the length of the time domain data should be longer than 100 ps. However, the measuring range in the time domain is limited to 25 ps in the experiment due to the Fabry-Pérot reflection signal from the rear surface of the silicon substrate. The oscillation and roughness of the transmission lines at some frequencies are attributed to the undesired system echoes of our laboratory-built THz-TDS equipment. Despite the limited resolution of measurement, the measured Q factors are still

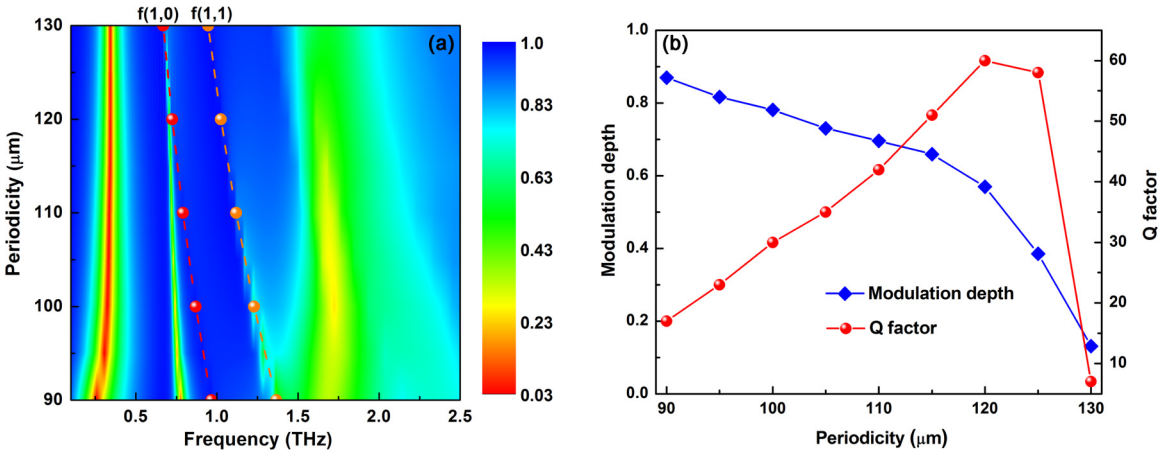

FIG. 3. (a) The amplitude transmission spectra of MM2 as a function of the periodicity. The red and yellow dotted lines mark the exact value at which the first- and second-order of diffraction modes. (b) Modulation depth (left scale) and Q factor (right scale) achieved of trapped-mode resonance f_2 when sweeping the periodicity (p) for the x-polarization.

higher than or comparable to that of most previous works in the THz region [23,26–28,31].

Besides those findings, it is worth mentioning that we observe another interesting effect when the periodicity p varies with other conditions unchanged. Figure 3(a) shows the transmission spectrum for the MM2 with periodicity p varying from 90 to 130 μm in steps of 5 μm as they are illuminated with x-polarization at normal incidence. A significant reshaping of the transmission spectrum of MM2 for different periodicities can be observed. The resonance f_2 is fairly weak and decreases rapidly for the periodicity over 120 μm. The sharpest resonance occurs for the critical period $p = 120\,\mu$m, and then a gradual broadening of the resonance f_2 is seen for lower periodicity. When the periodicity gradually decreases, the resonance f_2 shows a slight blueshift and becomes more prominent with a larger modulation depth. A noteworthy observation is the emergence of another abrupt resonant mode at higher frequency as the periodicity decreases, which indicates that the new resonance mode is different in nature from the localized eigenmode of SRR.

In addition, since the transmission spectra are highly dependent on the periodicity of the MM array, the effect of the periodicity (p) on the evolution of the Q factor and modulation depth for the particularly interesting resonance f_2 is retrieved. Figure 3(b) shows the modulation depth (left scale) and the Q factor (right scale) as a function of the periodicity with x-polarization. The Q factor increases dramatically as the periodicity changes from 90 to 120 μm while the modulation depth decreases gradually to 57% at a periodicity of 120 μm. For the periodicity above the threshold ($p = 120\,\mu$m), the resonance rapidly collapses, which leads to the degradation of the Q factor and a lower modulation depth. While simultaneously maximizing both the Q factor and modulation depth of the resonances is desirable, our results show that there is a trade-off between the maximum of the Q factor and the modulation depth. For the current geometry, the modulation depth monotonically decreases from 87% to 13% with the periodicity p increased from 90 to 130 μm, while the value of the Q factor achieves its maximum at $p = 120\,\mu$m with a value of 60. For our study, the mirror-symmetric arrangement of JSRR and the periodicity p are of crucial importance in achieving such an ultrahigh Q factor trapped-mode resonance.

IV. PHYSICAL ANALYSIS AND DISCUSSIONS

In general, there exist two fundamental electromagnetic coupling mechanisms in the periodic MM structures. One mechanism is the near-field electromagnetic coupling between localized plasmon resonances supported by the MM structures, which usually involves plasmon hybridization [17,22,24,35–37]. These plasmonic resonances are naturally independent on the periodicity of the MM arrays. The other mechanism is based on the interaction between the localized plasmon resonant mode and surface propagation modes such as surface plasmon polaritons or lattice surface modes, which are intrinsically correlated with the periodicity and the incident angle of the electromagnetic wave [38–40].

The underlying physics of the observed phenomenon in our MM structures can be well depicted by the diffraction coupling of localized surface plasmon resonances and near-field mirror-symmetric coupling in the mirrored JSRRs. It is well known that the arrangement of metallic subwavelength structures into a periodic lattice can give rise to an in-plane propagating collective lattice surface mode, which can cause abrupt changes in transmission near the Wood-Rayleigh anomaly [41,42]. For a rectangular array, the order of the diffracted wave and its corresponding frequencies can be defined by

$$k^2 = i^2\left(\frac{2\pi}{p_x}\right)^2 + j^2\left(\frac{2\pi}{p_y}\right)^2, \tag{1}$$

where $k = \frac{\omega}{v} = \frac{n\omega}{c}$ is the wave number of the scattered light, v is the speed of light in the surrounding medium with a refractive index of n, and (ij) is a pair of integers indicating the diffraction order. In our designs, the periods in the x and y axis are the same ($p_x = p_y = p$). Therefore, Eq. (1) can be expressed as

$$f = \frac{c\sqrt{i^2 + j^2}}{np}, \tag{2}$$

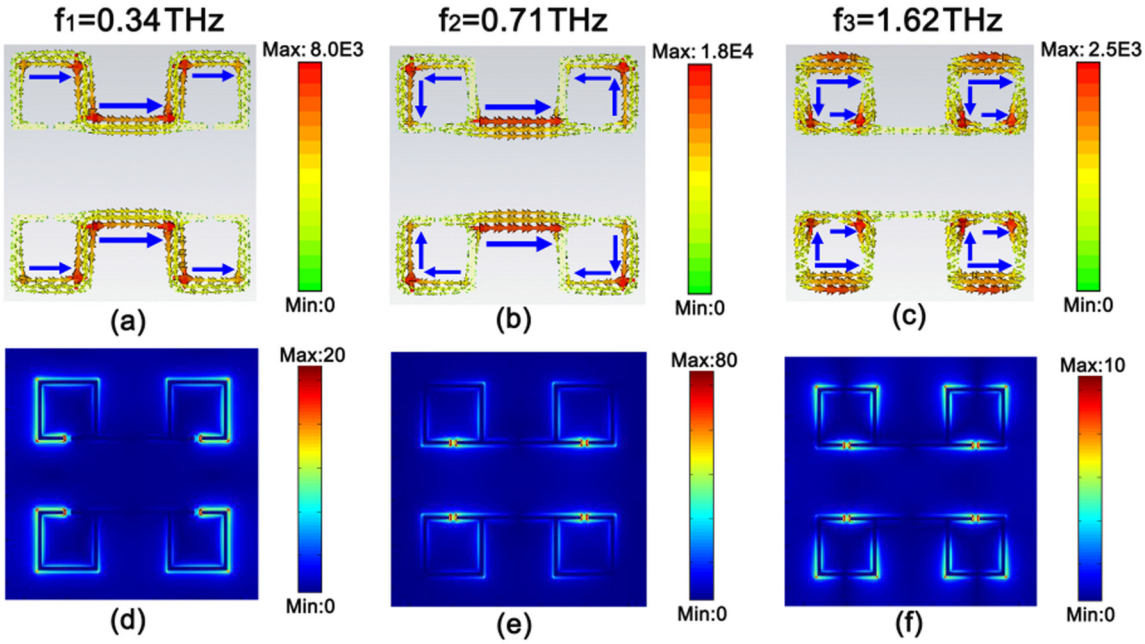

FIG. 4. Surface current and electric distribution for the MM2 structure at (a) and (d) dipolar-nature resonance f_1, (b) and (e) sharp trapped-mode resonance f_2, and (c) and (f) quadruple resonance f_3. These plots are taken from the midheight plane of the metallic structure. The simulation results of current and electric field intensities are in arbitrary units (color coded). Notice the scale bars in (b) and (e) are much larger than the ones in (a), (c) and (d), (f).

where f is the frequency of the corresponding diffracted wave. The MM array is oriented along the x and y axis and the incident wave propagates along the z axis. For zero-order diffracted waves, the constructive interference of scattered fields only occurs in the forward and backward directions, and thus radiates into free space, while first-order diffracted waves ($i = 1$, $j = 0$), under the condition of $f = c/np$ [9,40], can interfere constructively along the surface of the substrate and hence interact with the MM structures [39,42]. Based on Eq. (2), we calculate the first- and second-order diffraction of MM2 with the periodicity varying from 90 to 130 μm, which is superimposed on the transmission spectra, as shown in Fig. 3(a). The Wood-Rayleigh anomaly for MM2 with a period of 120 μm occurs at 0.72 THz, which is roughly equal to the frequency of f_2 in both simulation and experiment. However, it is worth noting that the Wood-Rayleigh anomaly arising from the array periodicity does not necessarily guarantee a sharp resonance in transmission [42]. Only if the Wood-Rayleigh anomaly frequency matches that of the localized surface plasmon resonance for individual MM structures can the diffracted waves strongly couple to the MM elements rather than to free space so that its energy can be strongly confined into the resonators. Therefore, under the condition that both the electric and magnetic dipole radiation components induced in the individual resonator are cancelled, the radiation damping can be drastically suppressed and the photon energy gets trapped in the lattices, leading to an ultrahigh Q factor. In our case, we employ a near-field mirror-symmetric coupling mechanism to cancel the dipole moment and minimize the radiation losses in the following.

In order to clarify the physical mechanism behind these spectral responses of mirror-symmetric JSRRs in greater detail, the surface current and electric field distributions of MM2 ($p = 120\,\mu$m) are calculated at the resonance frequencies as shown in Fig. 4. Although it is difficult to quantify the radiation of the structure analytically, the mechanism of the sharp resonance can be qualitatively interpreted by checking the radiation of the surface electric current. The induced current on the SRRs and metallic microstrip bridges can be schematically illustrated by several electric current elements, and these elements can be treated as electric dipoles which radiate electromagnetic waves to the far field. Subsequently, the basic multipole theory in electromagnetic scattering and radiation [43] is employed to elucidate the physical origin of the high Q factor resonance. For a localized electric current element $\vec{J}$, the relevant vector potential $\vec{A}$ at position r can be expressed as

$$\vec{A}(\vec{r}) = \frac{\mu_0}{4\pi}\int \frac{\vec{J}(\vec{r}')e^{ik|\vec{r}-\vec{r}'|}}{|\vec{r}-\vec{r}'|}d\vec{r}', \tag{3}$$

where $\vec{J}(\vec{r}')$ indicates the current distribution of the electric current element, and $k = \omega/c$ is the wave number. Its asymptotic form

$$\lim_{r\to\infty}\vec{A}(\vec{r}) \approx \frac{\mu_0}{4\pi r}e^{ikr}\int \vec{J}(\vec{r}')e^{-ik\vec{n}\cdot\vec{r}}dr' \equiv \frac{\mu_0}{4\pi r}e^{ikr}\vec{p} \tag{4}$$

is valid in the far field by approximating $|\vec{r}-\vec{r}'|$ as $r - \vec{n}\cdot\vec{r}$ in the numerator while in the denominator $|\vec{r}-\vec{r}'|$ is substituted by r. It follows that the far-zone radiated electromagnetic fields of the electric current element can be expressed by

$$\vec{B}_{\rm rad}(\vec{r}) = \frac{ik\mu_0}{4\pi r}e^{ikr}\vec{n}\times\vec{p}, \quad \vec{E}_{\rm rad}(\vec{r}) = c\vec{B}_{\rm rad}\times\vec{n}. \tag{5}$$

The time-averaged power radiated per unit solid angle by the oscillation dipole moment $\vec{p}$ is

$$\frac{dP_{\rm rad}}{d\Omega} = \frac{1}{2}{\rm Re}[r^2\vec{n}\cdot\vec{E}\times\vec{H}^*] = \frac{c^2Z_0}{32\pi^2}k^4|(\vec{n}\times\vec{p})\times\vec{n}|^2, \tag{6}$$

where $Z_0 = \sqrt{\mu_0/\varepsilon_0}$ is the intrinsic impedance of free space. The derivations above clearly demonstrate that the radiation loss is dominated by the direction-dependent vector $\vec{p}$ or, equivalently, the electric current element $\vec{J}$. In the mirror-symmetric coupled JSRR system, the current elements in the mirror-arranged JSRRs along the y direction always oscillate (π) out of phase due to the symmetry constraints, such that the dipole moment induced by the current elements in the y direction can be nearly canceled. Indeed, both the electric and magnetic dipole radiations of the currents oscillating in the vertical neighboring SRR are canceled. On the other hand, the electric current elements along the x direction in the four SRRs always oscillate in phase, which causes very high radiation losses. However, the electric current elements in the introduced metallic microstrip bridges support two types of oscillation modes. At the broadband resonance f_1, all the surface current elements in the x direction oscillate in phase and the radiated electromagnetic fields interfere constructively, as shown in Figs. 4(a) and 4(d). This indicates that the resonance f_1 is strongly coupled to free space, which contributes to the formation of a broad dipolar resonance with a high radiation loss and a very low Q factor. For the ultrasharp resonance f_2, the electric current elements in the introduced metallic microstrip bridges oscillate out of phase with respect to that of the horizontal SRR arms in the x direction, leading to the direct cancellation of the net dipole moment, accompanied with destructive interference of the scattered field [see Figs. 4(b) and 4(e)]. Therefore, in this case, the mirror-symmetric JSRR system ensures that nearly all the electric and magnetic dipole radiation components of current elements induced in the structure can be completely canceled in all directions via destructive interference. Hence, the radiation damping is exceedingly suppressed and the photon energy is strongly confined into the structure, eventually resulting in an ultrahigh Q factor resonance with a large modulation depth. For the third resonance f_3, a classical quadrupole resonance can be observed, and the surface currents as well as the electric field confinement shown in Figs. 4(c) and 4(f) are very weak. The strength of the induced currents and electric field of the trapped-mode resonance frequency f_2 is nearly one order of magnitude larger than those of f_3, which confirms that the photon energy is trapped in the lattice, and the radiation loss is significantly reduced. In essence, mirror-symmetric coupling plays an essential role in exciting such a trapped-mode resonance in this coupled JSRR system, because the net dipole moment can be greatly reduced in this case.

Based on the theoretical analysis above, the slight blueshift and broadening of the resonance f_2 as the period changes from 120 to 90 μm can be attributed to the mismatch between the localized surface plasmon resonance and lattice surface mode. The localized surface plasmon resonance for individual mirror-symmetric JSRR occurs at about 0.71 THz and the frequency of the lattice surface mode changes as the periodicity varies. The Q factor of resonance f_2 decreases as the frequency of the lattice surface mode for the MM array is shifted away from the localized surface plasmon resonance at about 0.71 THz. The appearance of the abrupt resonance mode is due to the second-order diffraction ($i = 1, j = 1$) of the MM2 array, because the theoretical and simulated results are perfectly matched, as shown in Fig. 3(a).

In addition, it is important to emphasize that cancellation of the dipole moment is maximized for the MM2 ($p = 120\,\mu$m) configuration. When the SRR gap is displaced inboard/outboard by 10.5 μm from the central axes of each SRR, the current strength and electric confinement at the trapped-mode resonance frequency are reduced, as shown in Fig. 5. For sample MM3 [Fig. 5(b)], the current distribution in the sidearms of SRRs is still out of phase with decreased amplitudes, thus the cancellation of the dipole moment in the vertical direction (y axis) is not affected. The current distributions in the metallic microstrip bridges, and the gap bearing arm of SRR become prominent at the resonance frequency, which enhances the radiation loss in the horizontal direction (x axis). This indicates a reduction of the Q factor of the trapped-mode resonance. For sample MM4 [Fig. 5(c)], it is interesting that the currents in the four SRRs are mainly confined in the sidearms of the SRRs, while the currents in the horizontal arms of SRRs become weaker. Therefore, the dipole radiation in the metallic microstrip bridges cannot be completely canceled, which yields a lower Q factor for this configuration. This further confirms that the near-field mirror-symmetric coupling and destructive interference of the electric and magnetic dipole radiations in the mirrored JSRRs play an important role in obtaining such a sharp resonance. On the other hand, modifying the gap position in the SRRs also changes the frequency of the localized surface plasmon

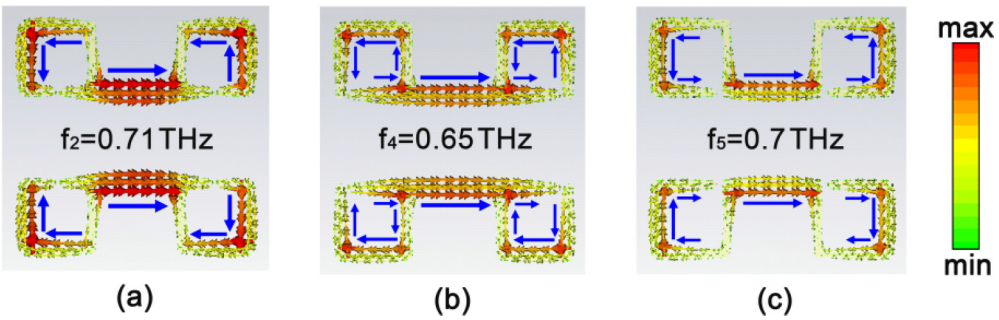

FIG. 5. Surface current distribution for the MM2, MM3, and MM4 structures at trapped-mode resonance (a) $f_2 = 0.71$ THz, (b) $f_4 = 0.65$ THz, and (c) $f_5 = 0.7$ THz, respectively.

resonance in mirror-symmetric JSRRs, and the mismatch between the frequencies of the localized surface plasmon resonance and lattice surface mode facilitates the degeneration of the Q factor of the trapped-mode resonance.

V. CONCLUSIONS

In conclusion, we demonstrate a mirror-symmetric JSRR structure that sustains an extremely sharp trapped-mode resonance with a large modulation depth. The strong interaction between the localized surface plasmon resonance in the mirror-symmetric JSRR and in-plane propagating collective lattice surface mode arising from the array periodicity drastically confines the photon energy into the lattice. The mirror-symmetric coupled JSRR leads to cancellation of the net dipole moment in all directions, accompanied by destructive interference of the scattered field, which significantly prevents the rapid radiative decay of photon energy from the structures and minimizes the radiation loss. This eventually leads to the formation of ultrasharp resonance near the Wood-Rayleigh anomaly frequency. By varying the array periodicity, the characteristic of the sharp-trapped resonance can be engineered, and multiple sharp plasmonic resonances can be obtained in the transmission spectra. Moreover, we also demonstrate that the Q factor and the resonance modulation depth can be tailored by controlling the gap position in individual resonators. This high Q factor MM may well enable great advances in applications such as ultrasensitive sensors, ultranarrow band filters, and optical switches. Our work would open up avenues for advanced design and realization of high-performance photonic devices in the technologically difficult terahertz regime.

ACKNOWLEDGMENTS

The authors acknowledge insightful discussions with Professor Shuang Zhang from the University of Birmingham. This work is supported by the National Natural Science Foundation of China under Grants No. 91323304, No. 11174362, No. 11504414, No. 11574385, No. 61390503, and No. 11374358, Strategic Priority Research Program of the Chinese Academy of Sciences under Grant No. XDB07020200, the Knowledge Innovation Project of CAS (Grant No. KJCX2-EW-W02), and the National Basic Research Program of China under Grant No. 2014CB339800.

[1] R. Singh, W. Cao, I. Al-Naib, L. Cong, W. Withayachumnankul, and W. Zhang, Appl. Phys. Lett. **105**, 171101 (2014).
[2] A. Cui, Z. Liu, J. Li, T. H Shen, X. Xia, Z. Li, Z. Gong, H. Li, B. Wang, J. Li, H. Yang, W. Li, and C. Gu, Light: Sci. Appl. **4**, e308 (2015).
[3] C. Wu, A. Khanikaev, R. Adato, N. Arju, A. Yanik, H. Altug, and G. Shvets, Nat. Mater. **11**, 69 (2012).
[4] A. Cetin and H. Altug, ACS Nano **6**, 9989 (2012).
[5] J. Hara, R. Singh, I. Brener, E. Smirnova, J. Han, A. Taylor, and W. Zhang, Opt. Express **16**, 1786 (2008).
[6] T. Driscoll, G. Andreev, and D. Basov, Appl. Phys. Lett. **91**, 062511 (2007).
[7] O. Paul, R. Beigang, and M. Rahm, Opt. Express **17**, 18590 (2009).
[8] H. Tao, A. C. Strikwerda, K. Fan, W. J. Padilla, X. Zhang, and R. D. Averitt, Phys. Rev. Lett. **103**, 147401 (2009).
[9] N. Born, I. Al-Naib, C. Jansen, R. Singh, J. V. Moloney, M. Scheller, and M. Koch, Adv. Opt. Mater. **3**, 642 (2015).
[10] N. Zheludev, S. Prosvirnin, N. Papasimakis, and V. Fedotov, Nat. Photonics **2**, 351 (2008).
[11] Y. Huang, W. Chen, P. Wu, V. Fedotov, N. Zheludev, and D. Tsai, Sci. Rep. **3**, 1237 (2013).
[12] N. Liu, L. Langguth, T. Weiss, J. Kästel, M. Fleischhauer, T. Pfau, and H. Giessen, Nat. Mater. **8**, 758 (2009).
[13] K. Totsuka, N. Kobayashi, and M. Tomita, Phys. Rev. Lett. **98**, 213904 (2007).
[14] S. Zhang, D. A. Genov, Y. Wang, M. Liu, and X. Zhang, Phys. Rev. Lett. **101**, 047401 (2008).
[15] R. Singh, I. Al-Naib, Y. Yang, D. Chowdhury, W. Cao, C. Rockstuhl, T. Ozaki, R. Morandotti, and W. Zhang, Appl. Phys. Lett. **99**, 201107 (2011).
[16] K. L. Tsakmakidis, M. S. Wartak, J. J. H. Cook, J. M. Hamm, and O. Hess, Phys. Rev. B **81**, 195128 (2010).
[17] C. Wu, N. Arju, G. Kelp, J. A. Fan, J. Dominguez, E. Gonzales, E. Tutuc, I. Brener, and G. Shvets, Nat. Commun. **5**, 3892 (2014).
[18] A. Barth and C. Zscherp, Q. Rev. Biophys. **35**, 369 (2002).
[19] S. Xiao, V. Drachev, A. Kildishev, X. Ni, U. Chettiar, H. Yuan, and V. Shalaev, Nature (London) **466**, 735 (2010).
[20] R. Singh, Z. Tian, J. Han, C. Rockstuhl, J. Gu, and W. Zhang, Appl. Phys. Lett. **96**, 071114 (2010).
[21] I. Al-Naib, Y. Yang, M. M. Dignam, W. Zhang, and R. Singh, Appl. Phys. Lett. **106**, 011102 (2015).
[22] V. A. Fedotov, M. Rose, S. L. Prosvirnin, N. Papasimakis, and N. I. Zheludev, Phys. Rev. Lett. **99**, 147401 (2007).
[23] R. Singh, I. Al-Naib, M. Koch, and W. Zhang, Opt. Express **19**, 6312 (2011).
[24] W. Cao, R. Singh, I. Al-Naib, M. He, A. J. Taylor, and W. Zhang, Opt. Lett. **37**, 3366 (2012).
[25] Y. Fan, Z. Wei, H. Li, H. Chen, and C. M. Soukoulis, Phys. Rev. B **87**, 115417 (2013).
[26] D. Chowdhury, X. Su, Y. Zeng, X. Chen, A. J. Taylor, and A. Azad, Opt. Express **22**, 19401 (2014).
[27] I. Al-Naib, C. Jansen, N. Born, and M. Koch, Appl. Phys. Lett. **98**, 091107 (2011).
[28] C. Jansen, I. Al-Naib, N. Born, and M. Koch, Appl. Phys. Lett. **98**, 051109 (2011).
[29] I. Al-Naib, E. Hebestreit, C. Rockstuhl, F. Lederer, D. Christodoulides, T. Ozaki, and R. Morandotti, Phys. Rev. Lett. **112**, 183903 (2014).
[30] T. Q. Li, H. Liu, T. Li, S. M. Wang, J. X. Cao, Z. H. Zhu, Z. G. Dong, S. N. Zhu, and X. Zhang, Phys. Rev. B **80**, 115113 (2009).
[31] I. Al-Naib, R. Singh, C. Rockstuhl, F. Lederer, S. Delprat, D. Rocheleau, M. Chaker, T. Ozaki, and R. Morandotti, Appl. Phys. Lett. **101**, 071108 (2012).
[32] D. Grischkowsky, S. Keiding, M. van Exter, and C. Fattinger, J. Opt. Soc. Am. B **7**, 2006 (1990).

[33] M. A. Ordal, R. J. Bell, R. W. Alexander, L. L. Long, and M. R. Querry, Appl. Opt. **24**, 4493 (1985).
[34] N. K. Grady, J. E. Heyes, D. R. Chowdhury, Y. Zeng, M. T. Reiten, A. K. Azad, A. J. Taylor, D. A. R. Dalvit, and H.-T. Chen, Science **340**, 1304 (2013).
[35] G. Vecchi, V. Giannini, and J. Gómez Rivas, Phys. Rev. B **80**, 201401(R) (2009).
[36] T. V. Teperik and A. Degiron, Phys. Rev. B **86**, 245425 (2012).
[37] E. Prodan, C. Radloff, N. J. Halas, and P. Nordlander, Science **302**, 419 (2003).
[38] C. J. Tang, P. Zhan, Z. S. Cao, J. Pan, Z. Chen, and Z. L. Wang, Phys. Rev. B **83**, 041402(R) (2011).
[39] A. Bitzer, J. Wallauer, H. Helm, H. Merbold, T. Feurer, and M. Walther, Opt. Express **17**, 22108 (2009).
[40] R. Singh, C. Rockstuhl, and W. Zhang, Appl. Phys. Lett. **97**, 241108 (2010).
[41] R. W. Wood, Phys. Rev. **48**, 928 (1935).
[42] V. G. Kravets, F. Schedin, and A. N. Grigorenko, Phys. Rev. Lett. **101**, 087403 (2008).
[43] J. D. Jackson, *Classical Electrodynamics*, 3rd ed. (Wiley, New York, 1999).